Journal of Catalysis **192,** 88–97 (2000)
doi:10.1006/jcat.2000.2834, available online at http://www.idealibrary.com on IDEAL®

Pd/MgO: Catalyst Characterization and Phenol Hydrogenation Activity

Peter Claus,*,[1] Heinz Berndt,* Christian Mohr,* Jörg Radnik,* Eun-Jae Shin,† and Mark A. Keane†,[1]

*Department of Catalysis, Institute for Applied Chemistry, Berlin-Adlershof e.V., D-12489 Berlin, Germany; and †Department of Chemical Engineering, The University of Leeds, Leeds LS2 9JT, United Kingdom

Received September 9, 1999; revised January 24, 2000; accepted January 24, 2000

The gas-phase hydrogenation of phenol ($423 \leq T \leq 573$ K) has been studied over a 1% w/w Pd/MgO catalyst prepared by impregnation of MgO with $(NH_4)_2PdCl_6$. The catalyst precursor was activated by precalcination in air at 473 K followed by reduction in hydrogen at 573 K. Temperature-programmed reduction/desorption (monitoring H_2 consumption and NH_3, H_2O, CO, and CO_2 release) has revealed the presence of ammonium carbonate and/or ammonium hydrogen carbonate on the active surface in addition to a metallic palladium component. Whereas the latter was not detectable by X-ray diffraction due to the high metal dispersion, transmission electron microscopy revealed that the mean palladium particle diameter is 1.3 ± 0.2 nm, which corresponds to a palladium dispersion of $D_{Pd} = 71\%$. Besides conventional and high-resolution transmission electron microscopy, selected area electron diffraction provides some insight into the fine structure of the palladium crystallites. Impregnation followed by calcination is shown to transform MgO to $Mg(OH)_2$ while the additional reduction step generates a surface phase that is composed of both needle-like Periclase MgO and $Mg(OH)_2$. X-ray photoelectron spectrometric analyses of the activated catalyst has established the presence of zero-valent palladium which appears to be electron rich as a result of metal–support interaction; a degree of palladium charging is also evident as well as residual surface chlorine. The effects on fractional phenol conversion and reaction selectivity of varying such process variables as reaction time, temperature, and phenol molar feed rate are considered and the possibility of thermodynamic limitations is addressed. Hydrogenation was observed to proceed in a stepwise fashion with cyclohexanone as the partially hydrogenated product and cyclohexanol as the fully hydrogenated product. The catalyst delivered a 96% selectivity with respect to cyclohexanone production at 423 K but the cyclohexanone yield decreased at higher temperatures as conversion declined and cyclohexanol was increasingly preferred. Conversion and selectivity were both stable with prolonged catalyst use, i.e., time on stream in excess of 55 h.

Key Words: **phenol hydrogenation; cyclohexanone; TPR/TPD analysis of Pd/MgO; XRD analysis of Pd/MgO; TEM analysis of Pd/MgO; XPS analysis of Pd/MgO.**

INTRODUCTION

Cyclohexanone is a key raw material (1, 2) in the synthesis of both caprolactam for nylon 6 and adipic acid for nylon 66. Cyclohexanone production, on a commercial scale, typically involves either the oxidation of cyclohexane or the hydrogenation of phenol (2). The former route requires high temperatures and pressures and generates appreciable byproducts that lower the cyclohexanone yield and complicate the recovery and separation stages. In the hydrogenation process, cyclohexanone can be obtained from phenol in a "one-step" or a "two-step" process. In the latter case, phenol is first hydrogenated to cyclohexanol (typically over a nickel catalyst) that is then dehydrogenated, in the second step, to yield cyclohexanone. A one-step selective direct hydrogenation to cyclohexanone is certainly preferable in terms of investment and energy savings as it avoids the endothermic dehydrogenation step. The development of a catalyst for this process has attracted a flurry of research activity. Palladium-based systems seem to show the most promise and a number of recent reports have emerged outlining activity/selectivity characteristics for the gas-phase reaction over a diversity of supported palladium catalysts (3–7). In most cases it has not proved possible to extract activity/selectivity data from the published results but the following is a representative list of the quoted (phenol conversion/cyclohexanone selectivity) optima: Pd/Al_2O_3, 40%/45% (3); $Pd/CaO–Al_2O_3$, 98%/20% (4); Pd/zeolite, 33%/44% (3); and Pd membrane, >75%/90% (5). While the above values span a wide range, the general trend suggests a drop in cyclohexanone selectivity at high phenol conversions. Promising results are now emerging (6, 7) with the use of hydrotalcite impregnated with $PdCl_2$ (to a Pd loading of 1% w/w) where a cyclohexanone selectivity of 92% has been achieved at a 98% conversion of phenol. Nevertheless, the attainment of a high selectivity (>95%) at elevated conversions (>70%) remains a challenging catalytic problem. The incorporation of promoters such as alkali (8, 9) and alkaline (9) metals has been shown to enhance selectivity while changes in reaction temperature (3, 5, 10) have had a considerable impact on the ultimate product composition.

[1] Authors to whom correspondence should be addressed.

0021-9517/00 $35.00

We report herein a catalyst system based on unpromoted palladium supported on MgO that does deliver the target cyclohexanone selectivity at a phenol conversion of 75%. The effects of varying such process variables as reaction time and temperature and phenol feed rate are considered while a comprehensive program of catalyst characterization (involving TPR/TPD, XRD, TEM, and XPS) gives some insight into the surface requirements for a high yield of cyclohexanone from a phenol feedstock.

EXPERIMENTAL

Catalyst Preparation, Activation, and Characterization

The Pd/MgO catalyst was prepared by impregnation of MgO (325 mesh, Aldrich) with an aqueous solution of $(NH_4)_2PdCl_6$ (Aldrich) and dried at 393 K for 8 h. The catalyst precursor was then calcined in flowing air (167 $cm^3\ min^{-1}$) at 473 K for 2 h and reduced in a 100 $cm^3\ min^{-1}$ stream of dry hydrogen (99.9%) at 573 K for 18 h. The Pd content (1% w/w) was determined by ICP-OES (Perkin Elmer Optima 3000XL); the quoted loading is the result of five independent measurements. Nitrogen physisorption measurements of the catalyst precursor at 77 K (Sorptomatic 1990, Fisons) yielded a specific surface area of 46 $m^2\ g^{-1}$, a pore volume of 0.46 $cm^3\ g^{-1}$, and an average pore diameter of 12 nm.

Catalyst reducibilty in a hydrogen/argon flow (after calcination) was probed by combined temperature-programmed reduction/desorption (TPR/TPD) using a conventional dynamic characterization system, AMI-1 (Altamira/Zeton), equipped with a thermal conductivity detector (TCD) and coupled to a quadrupole mass spectrometer QMG 420 C (Balzers) operating in the multiion-detection mode (MID). The TPR was conducted by heating a sample (0.3 g, particle size = 0.8–2.5 mm) at 10 K min^{-1} to 1073 K in a 30 $cm^3\ min^{-1}$ H_2/Ar flow and completing the activation with an isothermal hold at the final temperature. Two reducing gases were employed, i.e., a low (1% v/v) and high (5% v/v) hydrogen content stream with the option of different coupling positions of the quadrupole mass spectrometer (QMS) gas inlet to the flow system of the AMI-1. In some cases, the gas flow to the QMS was taken directly downstream of the AMI-1 reactor in order to monitor the overall product composition of the exiting gas. Desorbing components such as water and carbon dioxide were completely removed from the gas flow before it reached the TCD by capture in a KOH trap to allow a measure of hydrogen consumption/desorption; there was minimal interference from CO and NH_3 as minor products of the TPR step. It was also possible to couple the QMS to the analytical port of the AMI-1, i.e., behind the TCD detector, which enabled an additional sensitive monitoring of the hydrogen consumption/desorption in the 1% v/v H_2/Ar flow. It should be noted that in the case of the 5% v/v H_2/Ar mixture, a splitting of the flow to the TCD and QMS resulted in a delayed response when compared to 1% v/v H_2/Ar. The TCD was calibrated for hydrogen consumption by pulsing known volumes of argon into the H_2/Ar flow and relating peak area to hydrogen concentration.

X-ray diffraction (XRD) analysis was conducted, on the sample calcined *in situ* in air at 473 K, using a URB 6 diffractometer (Seifert FPM) with monochromatic Cu $K\alpha$ radiation. The effects of a cycle of sample reduction at 573 K and a further exposure to air were also monitored by XRD. The mean crystallite sizes were calculated from line broadening using the Scherrer equation. The activated samples were characterized by conventional (CTEM) and high-resolution transmission electron microscopy (HRTEM); CTEM and HRTEM analyses were conducted using a JEM 100C (accelerating voltage = 100 kV) and a JEM 4000EX (accelerating voltage = 400 kV), respectively. The specimens were prepared by dispersing the catalyst in *iso*-propanol with ultrasonic agitation and depositing small quantities of the resultant suspension on microgrids coated with thin, holey carbon films (Plano). Selected area electron diffraction (SAED) was used to confirm the crystal structure and crystallinity of the surface metal and the support. A combination of bright-field and dark-field imaging served to distinguish the contrast features of metal particles and the finely divided support components and facilitated an evaluation of the size and shape of the Pd particles. Micrographs were recorded using optimum imaging conditions (near Scherzer focus) and were subjected to digital image processing for contrast enhancement and image evaluation (software Digtal Micrograph by GATAN and NIH Image (12)).

X-ray photoelectron spectroscopic (XPS) analyses were conducted employing both monochromatized Al $K\alpha$ (1486.6 eV) and non-monochromatized Mg $K\alpha$ (1253.6 eV) radiation with a VG ESCALAB 220i XL energy analyzer. In the case of the Al $K\alpha$ source, data acquisition was carried out using a floodgun (8 eV) to reduce sample charging and the peaks were corrected, for energy referencing, to the C 1*s* signal of graphite with an assigned binding energy of 284.5 eV (12). The catalyst was calcined and reduced as described above in a reaction cell installed in the lock to the analysis chamber. For comparative purposes, pure MgO as used for catalyst preparation and a Pd reference catalyst (23% w/w Pd/MgO) were analyzed by XPS after the same activation procedure.

Catalytic Procedure

All the catalytic reactions were carried out under atmospheric pressure in a fixed-bed glass reactor (13) (i.d. = 15 mm) over the temperature range $423 \leq T \leq 573$ K. The catalyst was supported on a glass frit and a layer of glass beads above the catalyst bed served as a preheating zone

and ensured that the reactants were vaporized and reached the reaction temperature before contacting the catalyst. A Merck-Hitachi LC-6000A pump was used to deliver the phenol feed at a fixed molar rate which had been carefully calibrated and the vapour was carried through the catalyst bed in a stream of purified hydrogen. A methanolic solution of phenol was used as feed where the standard reaction conditions involved a phenol/methanol mole ratio of 1/4, hydrogen/phenol mole ratio of 20/1, and an overall space velocity of 800 $g_{phenol}\ h^{-1}\ (l_{catalyst})^{-1}$. The molar aromatic feed rate was, however, varied in the range 4.9×10^{-3}–4.4×10^{-1} mol h^{-1} to deliver W/F values of 11–101 g mol^{-1} h where F is the molar feed rate and W the weight of catalyst. The nature of the alcoholic solvent has been shown to have a bearing on the hydrogenation rate where rate is lowered in the presence of higher straight-chain alcohols (particularly 1-hexanol/1-heptanol); this polarity effect is taken to be indicative of the contribution of phenoxide ion/catalyst interactions in promoting the reaction (13). Passage of both the methanolic solutions of phenol in a stream of hydrogen through a fixed bed of glass beads (in the absence of Pd/MgO) and methanol itself through the catalyst bed over the same temperature range did not result in any measurable conversions. The catalyst system was operated with negligible internal or external diffusion retardation of reaction rate (effectiveness factor >0.99) and heat transport effects can be ignored. Catalyst deactivation was probed by ascending and subsequent descending reaction temperature sequences over the entire temperature interval that was studied. In addition, one standard set of reaction conditions ($T = 473$ K, $W/F = 69$ g mol^{-1} h) was routinely repeated to ensure that the catalyst had not suffered any long-term deactivation. The reactor effluent was frozen in a liquid nitrogen trap for subsequent analysis which was made using an AI Cambridge GC94 chromatograph equipped with a flame ionization detector and employing a DB-1 50-m × 0.20-mm-i.d., 0.33-μm capillary column (J&W Scientific). Data acquisition and analysis was performed using the JCL 6000 (for Windows) chromatography data system and product distribution was converted to mole fraction using detailed (20-point) calibration plots; the lower limit of quantitative analysis represents a 0.1% conversion of the feedstock. Catalytic action is discussed in this paper in terms of fractional conversion (x), percentage selectivity (S), and percentage yield (Y) where, for the production of cyclohexanone from phenol,

$$x_{C_6H_5OH} = \frac{[C_6H_5OH]_{in} - [C_6H_5OH]_{out}}{[C_6H_5OH]_{in}} \quad [1]$$

$$S_{C_6H_{10}O}(\%) = \frac{[C_6H_{10}O]_{out}}{[C_6H_5OH]_{in} - [C_6H_5OH]_{out}} \times 100 \quad [2]$$

$$Y_{C_6H_{10}O}(\%) = \frac{[C_6H_{10}O]_{out}}{[C_6H_5OH]_{in}} \times 100, \quad [3]$$

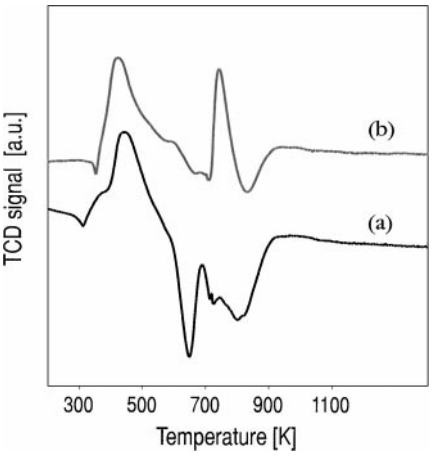

FIG. 1. TPR plots obtained for the reduction of Pd/MgO in (a) 1% v/v H_2/Ar and (b) 5% v/v H_2/Ar.

and [ ] denotes the concentration of the pertinent organic. All the reactants were AnalaR grade and were used without further purification.

RESULTS AND DISCUSSION

The Nature of the Active Catalyst

The TPR profiles, generated from the TCD output, for the two reductive flows (1% v/v and 5% v/v H_2 in Ar) are shown in Fig. 1, where hydrogen consumption appears as a positive peak and hydrogen desorption as a negative peak. The QMS output from the TPR in 1% v/v H_2/Ar is given in Fig. 2, which illustrates the temperature dependence

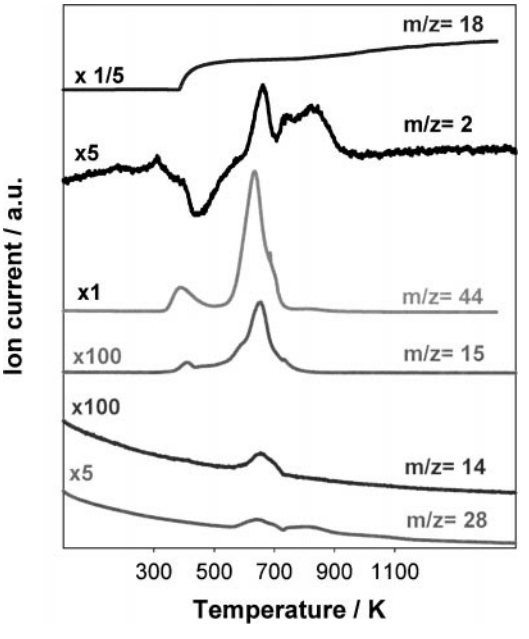

FIG. 2. QMS output during the TPR of Pd/MgO in 1% v/v H_2/Ar.

of the signals for hydrogen ($m/z = 2$), ammonia ($m/z = 15$ (14)), water ($m/z = 18$), carbon monoxide ($m/z = 28$ (14)), and carbon dioxide ($m/z = 44$). Positive peaks in the ion current plots reveal a desorption while negative peaks, in the case of hydrogen, imply consumption. Both the TCD and the QMS outputs for hydrogen coincide in the case of TPR in the low hydrogen content reducing flow. It should, however, be noted that, while the TCD plot is mainly determined by the changes in hydrogen concentration, the small amounts of CO (and NH_3 to an even lesser extent) that were liberated by the catalyst at $T > 600$ K contribute slightly to the negative peak response in the TCD plot. The low-temperature negative peak (T_{max} below 350 K) that appears in both profiles in Fig. 1 is entirely reproducible and is diagnostic of a metallic palladium component that is formed during the calcination step. The desorbing hydrogen may be present as a chemisorbed species on the surface or absorbed in the bulk of the metallic palladium particle, i.e., β-Pd/hydride formation. While the reduction of the supported palladium appears to commence at ca. 353 K, β-Pd/hydride decomposition may well occur concomitantly with hydrogen consumption. The hydrogen consumption calculated from the area of this peak ($T_{max} = 422$ or 440 K) amounts to ca. 45 and ca. 67 μmol g^{-1} for profiles a and b, respectively. This hydrogen consumption peak may represent the hydrogen that is required for PdO reduction and/or hydrogen chemisorption on the metallic palladium that is formed and/or hydrogen adsorption that is known to occur directly on the MgO (14) as well as spillover species. As the resultant output is such a composite value, it is not possible to extract a measure of the degree of reduction of palladium directly from the TPR data. The TCD response for both reductive flows is different at $T > 600$ K. A negative peak ($T_{max} = 653$ K) in profile a is diagnostic of hydrogen release while profile b is characterised by a sharp positive TCD peak ($T_{max} =$ ca. 743 K) revealing an additional hydrogen consumption. There are a number of possible explanations to account for the complex interplay between hydrogen consumption and release in the temperature range $500 \leq T \leq 800$ K and the related gas-phase hydrogen concentration dependence. On the one hand, both negative peaks in profile a could result from a desorption of hydrogen on both palladium and magnesia. On the other hand, the release of hydrogen represented by the negative peak at $T_{max} = 653$ K may be the result of a reoxidation of highly dispersed palladium in the hydrogen dilute stream by adsorbed water or surface hydroxyl groups on the magnesia surface corresponding to Eqs. [4] and [5]:

$$Pd + H_2O \rightarrow PdO + H_2 \quad [4]$$

$$Pd + 2OH^- \rightarrow PdO + O^{2-} + H_2. \quad [5]$$

The second positive peak at ca. 743 K in profile b clearly reveals a further hydrogen consumption that is also observed in profile a to a far lesser degree at the same temperature maximum. It is probable that hydrogen activated on metallic palladium spills over onto the MgO support where it is desorbed at higher temperatures, giving rise to the second negative peak above 800 K in both profiles. Hydrogen adsorption at low temperatures on thermally activated MgO has been reported by Ito *et al.* (15, 16) where a heterolytic dissociation of the hydrogen molecule was proposed; seven desorption peaks were observed between 200 and 650 K. Recently, dissociative adsorption of hydrogen on nanostructured and structurally disturbed MgO was reported (17) which was also found to result in the formation of Mg_sH and Mg_sOH species on the magnesia surface.

Taking the QMS profiles in Fig. 2, the desorption of water ($m/z = 18$) and carbon dioxide ($m/z = 44$) from MgO is not unexpected, arising from H_2O/CO_2 adsorption during sample handling while the magnesia as supplied contained carbonate. The occurrence of two peaks for CO_2 ($T_{max} = 413$ and 633 K) suggests a release from different adsorption sites or states. A TPD of CO_2 from MgO has been reported by Zhang *et al.* (18) where the principal loss occurred between room temperature and 473 K, a weak desorption peak was observed at ca. 523 K, and desorption reached completion only at temperatures in excess of 673 K. Tsuji *et al.* (19), employing IR spectroscopy and TPD with ^{18}O-labeled CO_2 to characterise the interaction of CO_2 with MgO, observed one desorption peak with a maximum around 800 K. They concluded that a surface bidentate carbonate species formed at room temperature can migrate on the surface as the temperature is raised during TPD. In our study, we noted the additional loss of carbon monoxide ($m/z = 28$) and, moreover, a secondary profile (at $m/z = 16$, CO fragment not shown in Fig. 2) that was closely similar, in terms of response, to the CO evolution. The CO liberation can be explained on the basis of a reverse water–gas shift reaction in the H_2/Ar flow via an oxygen delivery from CO_2 adsorbed on the oxygen vacancies of MgO. Finally, the profile at $m/z = 15$ is indicative of residual ammonium on the surface that is present in the precursor (prepared by using $(NH_4)_2PdCl_6$); nitrogen loss can, however, be excluded because no relationship between the plots for $m/z = 28$ and $m/z = 14$ was evident. The $m/z = 14$ profile can be ascribed to a superimposition of the ion current profiles of N^+ and CO^{2+}. The synchronous shape of the profiles for CO_2 ($m/z = 44$) and NH_3 ($m/z = 15$) desorption supports the presence of ammonium carbonate and/or ammonium hydrogen carbonate on the catalyst.

The XRD patterns, shown in Fig. 3, reveal the presence of $Mg(OH)_2$ with a mean crystallite size of 11.2 nm in the case of the calcined Pd/MgO sample (see profile a). Aqueous impregnation with the acidic palladium precursor salt resulted in an almost complete transformation of MgO to $Mg(OH)_2$ which appears to be stable under calcination

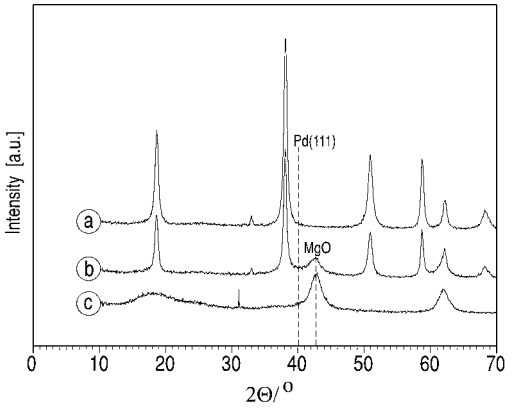

FIG. 3. XRD patterns for the Pd/MgO sample after calcination in air at 473 K (a) followed by reduction in hydrogen at 573 K with (b) or without (c) contact to air.

conditions at 473 K. It has, however, been established (20) that an evolution of H_2O and CO_2 from $Mg(OH)_2$ is observed only at temperatures in excess of 700 K. Reduction of the Pd/MgO in hydrogen at 573 K followed by contact with air generated a (poorly) crystalline MgO phase (mean crystallite size = 4.8 nm) in addition to the hydroxide (mean crystallite size = 12.2 nm); see profile b. A direct reduction (again at 573 K) of the calcined sample but without subsequent contact to air resulted in the formation of pure MgO (mean crystallite size = 4.0 nm), as shown in profile c. It must be noted that in each case there was no detectable palladium phase which suggested that either the palladium particle size is lower than 3 nm, the resolution limit of the diffractometer, or the palladium content of the catalyst (1 wt%) was too low to yield an XRD pattern. The TEM analysis has, however, confirmed that this apparent absence of a palladium crystalline phase is due to the high degree of Pd dispersion. The precalcined/reduced Pd/MgO sample was analysed by conventional transmission electron microscopy (CTEM) with selected area electron diffraction (SAED) and high-resolution transmission electron microscopy (HRTEM). The support was found to consist of a more or less amorphous component with an appreciable amount of crystalline needle-like structures, shown in Fig. 4. The TEM bright-field analysis served to reveal that the Pd is present in a highly dispersed form with the majority of particles in the size range 1–2 nm. Moreover, as is shown in Fig. 5, the palladium particles exhibit a narrow size distribution with a low mean particle size (1.3 ± 0.2 nm). It should be noted that this size distribution does not include those areas wherein the palladium particles appeared to form "clumps" but as this was, by no means, a common feature the quoted mean Pd particle size should not differ significantly from that which would be extracted from a consideration of the size distribution of the entire palladium content. Based on the mean particle size the palladium

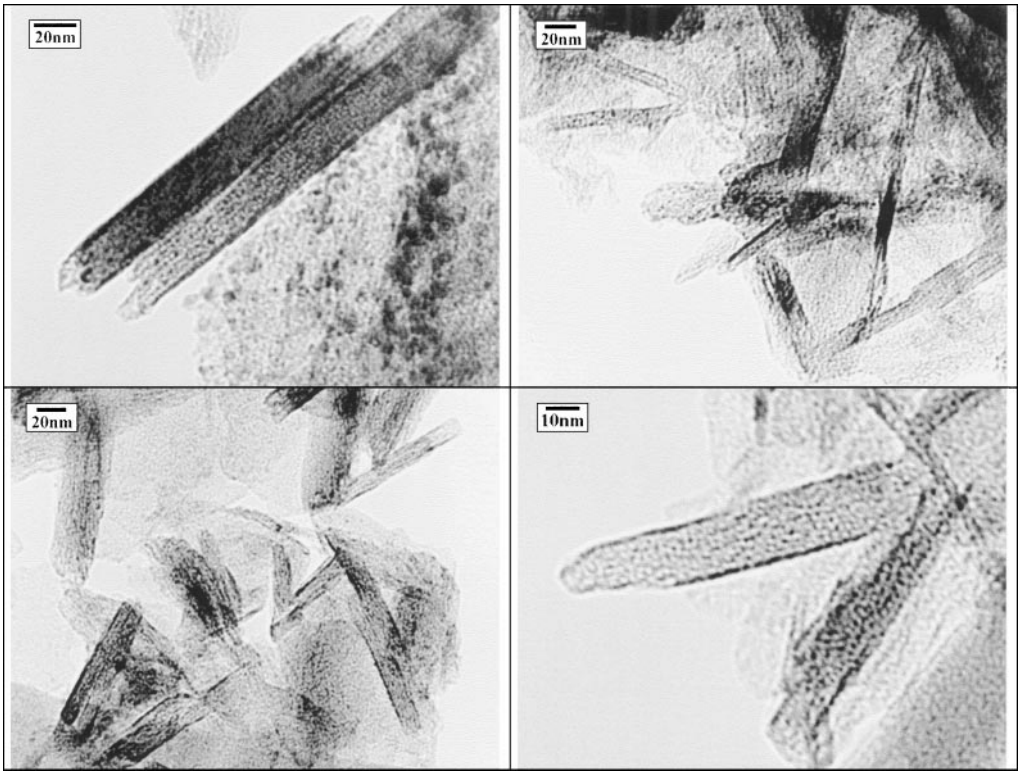

FIG. 4. Representative TEM images of the activated (precalcined/reduced) Pd/MgO sample.

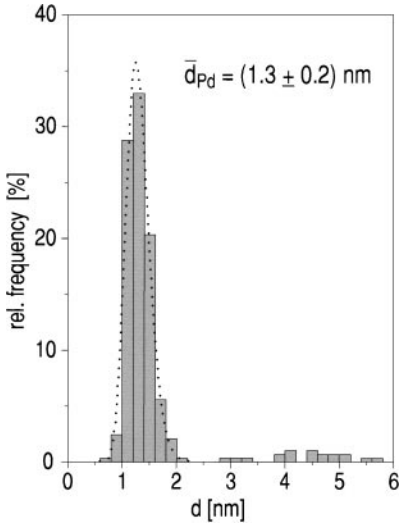

FIG. 5. Size distribution of the supported Pd particles: log-normal fit is shown by the dashed line.

dispersion was estimated to be 0.71 ± 0.05 assuming a spherical particle shape.

Diffraction patterns characteristic of MgO and $Mg(OH)_2$ were clearly observed by SAED, and are shown in Fig. 6, for every selected area of sample that was examined. Compared with the XRD measurements (see Fig. 3), a higher intensity of diffraction spots for MgO relative to $Mg(OH)_2$ was found by SAED. This may be attributed to a suppression of the hydrophilic properties of MgO due to the high-vacuum conditions employed during SAED. As the supported palladium is present as such small crystallites, no appropriate spots were found in the SAED analysis. It should be noted that analysis of a used sample did not reveal

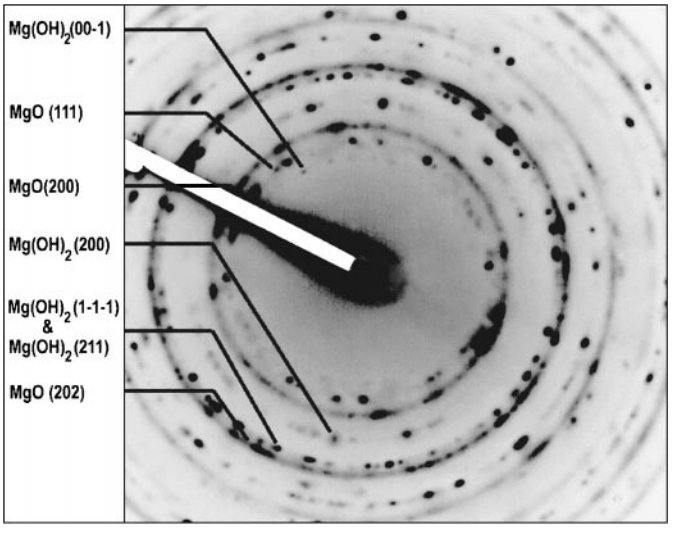

FIG. 6. Representative SAED image: the origin of the different diffraction spots and rings is indicated.

any marked differences from the freshly activated Pd/MgO. The average Pd particle size was, however, shifted to the slightly higher mean value of 1.8 nm as a result of the catalytic step. It was necessary to employ HRTEM in order to characterize the lattice structure of the supported Pd and the MgO carrier. By resolving lattice distances of single particles it was possible to determine each phase that is present on the active surface. Quantitative measurements were carried out by computing the Fourier transformation (FFT, NIH image software (11)) of the selected area of interest in the digitized image and measuring the spot distances; the latter can be taken to be the reciprocal of real distances. Calibration of the absolute magnification of the microscope was realized by measuring lattice distances of bulk Au(111). A careful quantitative analysis of a large number of particles, including comparison with known data (21) and diffraction simulations, yielded a lattice distance of 0.225 nm (with a maximum associated error of 0.005 nm) which is characteristic of metallic particles consisting of single crystalline fcc palladium (lattice distance Pd(111) = 0.22458 nm). It should be noted that some larger particles with well-developed defect structures were also present. While it is certain that the measured lattice distances belong to Pd(111), it is important to note that the spots in the Fourier transformation were noticeably broadened, indicative of a strong variation of the lattice distances within one particle. Moreover, HRTEM (see Fig. 7) revealed that the needle-like support structure is composed of Periclase MgO while the remainder of the support was identified as $Mg(OH)_2$.

An overview of the XP spectrum (Al $K\alpha$ source) for the Pd/MgO sample, following the standard (precalcination/reduction) activation procedure, is provided in Fig. 8a. The survey spectrum reveals the main components of the activated surface. The position of the Mg 2*p* peak at 49.2 eV points to the presence of $Mg(OH)_2$. The signal at 198 eV is attributed to residual chlorine that remains on the surface after the decomposition of the Pd precursor. As the chlorine signal in the reduced catalyst is of higher intensity than that in the calcined sample (not shown), segregation of chlorine from the bulk to the catalyst surface by pretreatment in flowing hydrogen must occur. The binding energy range between 320 and 355 eV, identified in Fig. 8a by an asterisk, is expanded in Fig. 8b, which also includes the spectrum for the calcined catalyst. The occurrence of the MgKL_1L_{23} peak originating from the catalyst support is unfortunate as it lies in the region of the $3d_{5/2}$ signal of Pd (335.1 eV), PdO (336.3 eV), and PdO_2 (337.9 eV) (12). As the peak around 335 eV is very broad and unsymmetrical, the superimposition of a signal due to a palladium component appears likely, particularly in the case of the reduced sample. Due to the dominance of the MgKLL Auger peaks between 300 and 350 eV it was expected that a deconvolution of this peak in the Al $K\alpha$ spectra would yield little of value. The Pd 3*d* peak was probed further by

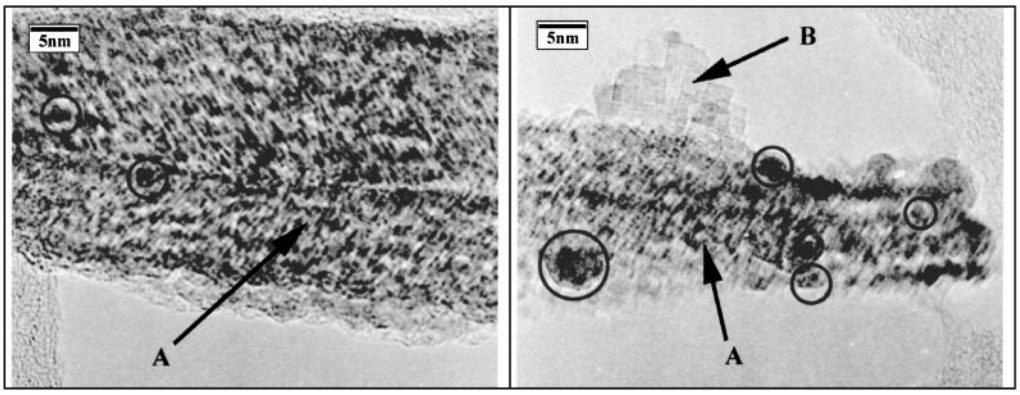

FIG. 7. HRTEM images: structures A and B, indicates with arrows, represent the MgO support; selected Pd particles are circled.

employing an Mg $K\alpha$ radiation source (1253.6 eV) in order to eliminate the MgKL_1L_{23} peak that masked the Pd binding energy range. The resultant XPS measurements for the calcined and precalcined/reduced samples are shown in Fig. 9. A four-peak system is observed for both calcined and reduced samples, spanning the range 330–350 eV. Two of these peaks with an associated binding around 335 and 340 eV can be positively assigned to Pd $3d_{5/2}$ and Pd $3d_{3/2}$. The Pd $3d_{5/2}$ binding energy (335.7 eV) of the calcined sample was shifted after reduction to a lower value (334.4 eV). The splitting of the signals of Pd $3d_{5/2}$ and Pd $3d_{3/2}$ were obtained to 4.9 and 5.5 eV for the calcined and reduced samples, and the peak ratio corresponds to the literature

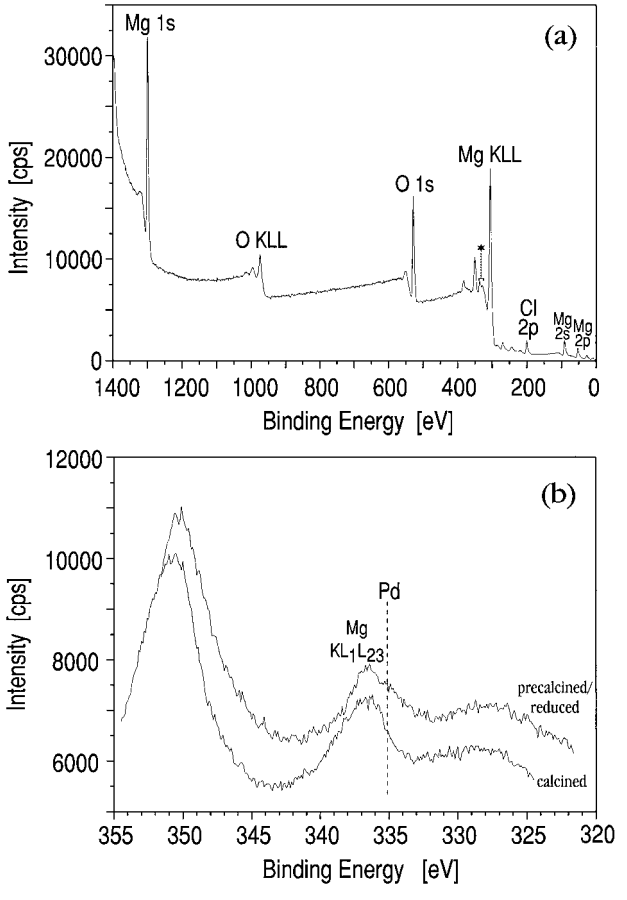

FIG. 8. (a) XPS (Al $K\alpha$ source) overview of the activated (precalcined/reduced) Pd/MgO sample. The region identified by the asterisk is expanded in (b) over the binding energy range 320–355 eV for the both the calcined and precalcined/reduced Pd/MgO sample.

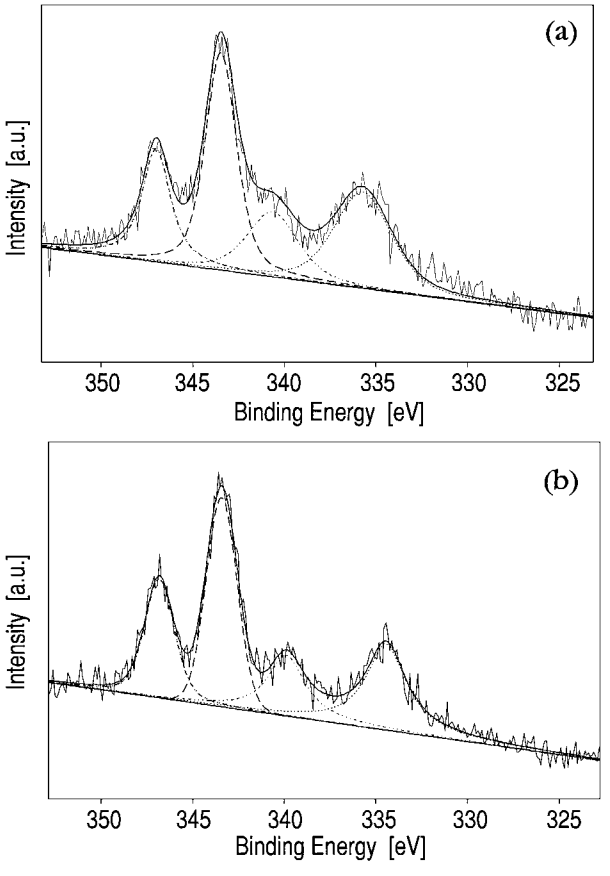

FIG. 9. XPS (Mg $K\alpha$ source) of the (a) calcined and (b) precalcined/reduced Pd/MgO sample.

TABLE 1

XPS Analysis of the Calcined (-C) and Precalcined/Reduced (-C/R) Pd/MgO Catalysts

	Catalyst	
	Pd/MgO-C	Pd/MgO-C/R
Pretreatment conditions	Calcination at 473 K	Calcination at 473 K, reduction at 573 K
Binding energy Pd $3d_{5/2}$ (eV)	335.7	334.4
Elements detected (at.%)		
Pd	0.3	0.5
Mg	30.4	32.3
O	60.7	59.8
C	8.5	4.5
Cl	Trace	3.0

value, i.e., 1.45 (12). The Pd $3d_{5/2}$ binding energies are given in Table 1 along with a quantitative estimation of the surface elements in the calcined and reduced samples. The observed (1.3 eV) shift to a lower energy after the reduction step corresponds to a change of the oxidation state of palladium from +2 to 0. Moreover, when their binding energy is compared with that of palladium bulk metal (335.1 eV), the magnesia-supported palladium particles (334.4 eV) appear to be electron-rich as a result of a metal–support interaction where an electronic ligand effect is induced by the support. Indeed, Mojet *et al.* (22) and Kappers *et al.* (23) have reported that the use of magnesia as a support leads to the formation of small electron-rich supported Pd and Pt particles. A decrease in the binding energy of Pd below the value for bulk Pd has also been observed for Pd/Y zeolite catalysts (24). The appearance of the two remaining peaks with binding energies of 343.5 and 347.0 eV for the calcined sample (see Fig. 10) that are very close to those (343.4 and

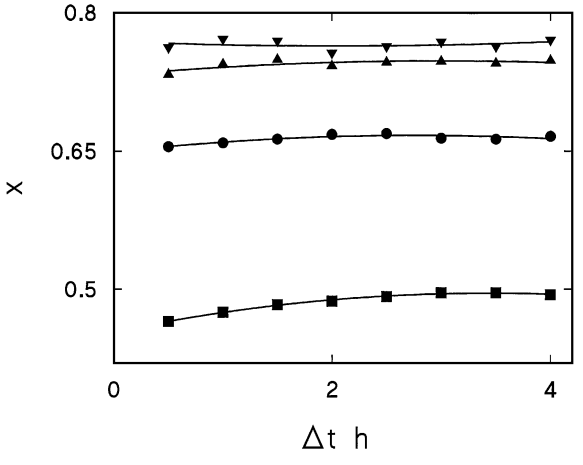

FIG. 10. Variation of the phenol fractional conversion (x) with time on stream at 573 K (■), 553 K (●), and 423 K over a freshly activated catalyst (▲) and at 423 K after processing a total of 1×10^4 mol of phenol per mole of palladium (▼); $W/F = 69\,\mathrm{g\,mol^{-1}\,h}$.

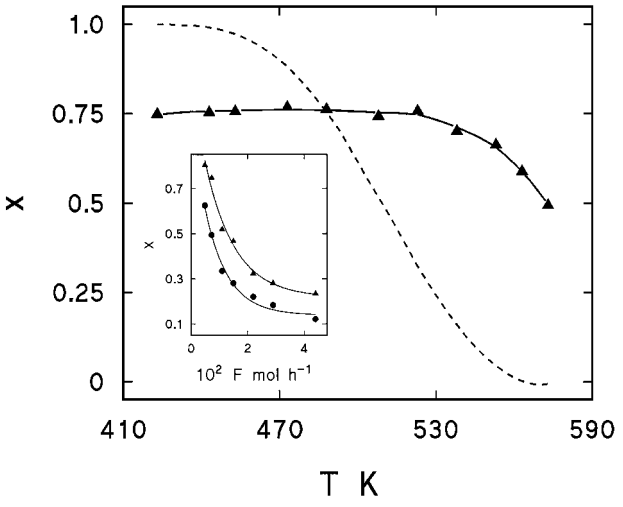

FIG. 11. Effect of reaction temperature on the fractional conversion of phenol (x) over Pd/MgO (▲) and that calculated from the temperature dependence of the reaction equilibrium constants (dashed line); $W/F = 69\,\mathrm{g\,mol^{-1}\,h}$. Inset: variation of fractional conversion (x) with phenol molar feed rate (F) at 423 K (▲) and 573 K (●).

346.8 eV) recorded for the reduced sample (see Fig. 11) is more difficult to explain. The possibilities of a contribution from an element other than palladium or a core level shift due to the small size of the supported Pd clusters can both be discounted. In the latter case, the energy difference between the two peak systems (nearly 9 eV) is far too great. One possible cause may be a charging of the Pd particles. In order to probe this effect, we determined the Auger parameter α (α = Pd $3d_{5/2}$ binding energy + Pd MVV kinetic energy), which is insensitive to charging effects, and compared those generated for a Pd/MgO reference catalyst which had a considerably higher Pd loading (23% w/w) and which was also pretreated using the standard conditions. The latter catalyst exhibited only two Pd peaks in the XP spectrum. Considering the relative uncertainty in the determination of the position of the broad Auger peaks, essentially the same values for the Auger parameter were obtained for both calcined and reduced samples to give an average value of $\alpha = 668.4 \pm 1.3$ eV. This is in accord with the suggestion of a charging effect of the highly dispersed Pd phase, a phenomenon that was largely unaffected by treatment with hydrogen.

The Catalytic Reaction

Cyclohexanone and cyclohexanol were the only reaction products observed over the entire temperature range that was studied, suggesting that the hydrogenation of phenol is stepwise with cyclohexanone as the partially hydrogenated product and cyclohexanol as the fully hydrogenated product. The MgO-based catalyst used in this study promoted only hydrogenation steps whereas Pd supported on acidic carriers has been shown (3, 8) to generate benzene,

cyclohexane, and dicyclohexylether, i.e., involvement of hydrodehydroxylation and condensation reactions. Phenol conversion was essentially independent of time on stream, as illustrated by the representative profiles shown in Fig. 10, and a steady-state conversion was readily achieved. A discernible induction period was apparent at higher reaction temperatures wherein conversion increased over the first two hours on stream before attaining a constant value. The deactivation reported for other palladium systems (5, 6, 8) was not observed in this study. Indeed, the same batch of catalyst after prolonged use (phenol/Pd mole ratio $>1\times10^4$) delivered a fractional conversion of phenol that was slightly higher (see Fig. 10) than that recorded for the freshly activated sample. The effect of reaction temperature on the fractional conversion of a fixed inlet molar phenol feed rate is presented in Fig. 11. Phenol conversion was essentially constant over the temperature interval $423 \le T \le 523$ K but did decline at more elevated temperatures. A drop in activity has been attributed elsewhere (8) to a temperature-induced decrease of the fraction of the catalyst surface that is covered by reactants. The possibility of thermodynamic limitations was considered by estimating the pertinent gas-phase reaction constants using the NIST database (25). The equilibrium constants (K_1 and K_2) for the stepwise hydrogenation of phenol can be presented in the form of a temperature dependence where

$$C_6H_5OH + 2H_2 \overset{K_1}{\rightleftarrows} C_6H_{10}O \qquad \log K_1 = \frac{6769}{T} - 13.3 \quad [6]$$

$$C_6H_{10}O + H_2 \overset{K_2}{\rightleftarrows} C_6H_{11}OH \quad \log K_2 = \frac{3332}{T} - 6.5. \quad [7]$$

The calculated gas-phase equilibrium conversion shows (see Fig. 11) a marked temperature dependence with complete conversion achieved at $T \le 443$ K and a continual drop thereafter to a residual conversion ($x < 0.03$) at 573 K. The catalytic system did not achieve equilibrium gas-phase conversions at $T < 493$ K, and while conversion in both cases declines at higher temperatures, the presence of the Pd/MgO catalyst ensured a consistently higher degree of conversion and maintained an appreciable level of activity up to 573 K. The catalytic data are clearly removed from gas-phase equilibrium conversions and the response of activity to changes in temperature can be attributed positively to surface reaction phenomena. Indeed, the degree of conversion was observed to drop with increasing inlet phenol feed rate as is illustrated in the inset to Fig. 11 for the two reaction temperature extremes.

The reaction equilibrium temperature dependences given in Eqs. [6] and [7] were used to calculate the equilibrium product compositions at representative temperatures, and the resultant reaction selectivities and yields in terms of cyclohexanone formation are compared in Fig. 12 with those generated in the catalytic process. The catalytic

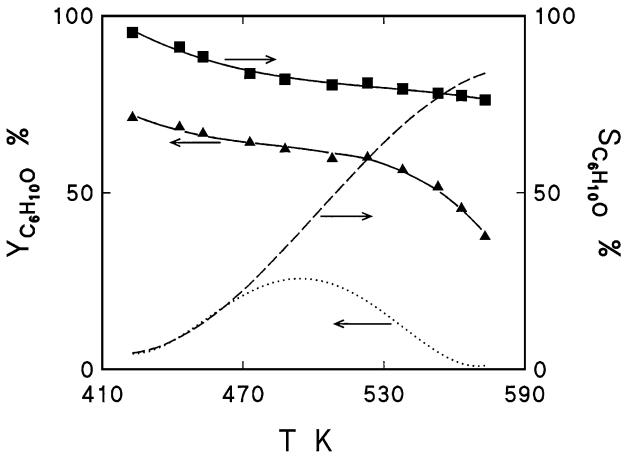

FIG. 12. Cyclohexanone selectivity (■/dashed line) and yield (▲/dotted line) as a function of reaction temperature where the data were generated in the catalytic step (symbols) or calculated from the temperature dependence of the reaction equilibrium constants (lines); $W/F = 69\,\mathrm{g\,mol^{-1}\,h}$.

and gas-phase equilibrium systems clearly diverge in terms of reaction selectivity. Under equilibrium conditions, cyclohexanol is the predominant product at lower reaction temperatures but cyclohexanone is increasingly preferred as the reaction temperature is raised. The opposing temperature dependences in terms of phenol conversion and cyclohexanone selectivity are seen to generate a maximum in cyclohexanone yield at 493 K. In complete contrast, the catalytic system generated cyclohexanone as by far the preferred product at lower temperatures, with a selectivity in excess of 95% at 423 K. This high selectivity was stable with prolonged catalyst use and the cyclohexanone selectivity/yield that was generated using the freshly activated sample was within 4% of the values generated after reaction times in excess of 55 h. Selectivity, and likewise yield, did however drop with a further increase in temperature as full hydrogenation to cyclohexanol was increasingly promoted. The source or surface requirement(s) for a high cyclohexanone selectivity has not been established in the literature and even the reaction mechanism is not well understood. Cyclohexanone can be generated from the hydrogen treatment of phenol by (a) direct hydrogenation or addition of two hydrogen molecules/four hydrogen atoms, (b) hydrogenation to cyclohexanol followed by a dehydrogenation step, or (c) formation of cyclohexen-1-ol followed by a tautomerism. A nonplanar mode of phenol interaction with the basic MgO support has been proposed (8) through the hydroxyl function as opposed to a coplanar surface arrangement which appears to predominate on acidic, e.g., Al_2O_3, supports involving a strong interaction with the aromatic nucleus. The former should favour a stepwise addition of hydrogen and high cyclohexanone selectivity (13). A one-site dissociative adsorption of both phenol and hydrogen on palladium has been proposed by Chen *et al.* (10) to favour

high cyclohexanone selectivities. It is not possible, from the combination of catalyst characterisation and catalysis data presented in this paper, to conclusively identify the predominant surface arrangment that leads to the high cyclohexanone selectivity recorded for this Pd/MgO catalyst which is, in turn, dependent on process conditions. The active catalyst is characterised by a high dispersion of electron-rich palladium crystallites ($D_{Pd} = 71\%$) which interact with the $MgO/Mg(OH)_2$ phase. The charge density at the metal site will certainly have a considerable bearing on the nature of the surface-activated hydrogen while the presence of the electron-withdrawing residual chlorine component may contribute to the active site(s). Indeed, Mahata and Vishwanathan (9) have shown that the *d*-character of supported palladium has a considerable influence on the progress of phenol hydrogenation. Moreover, palladium has a high intrinsic double bond isomerisation activity (26) which may be further enhanced in this catalyst and this will certainly promote cyclohexanone formation via step c. The combination of high and stable activity and selectivity at a low operating temperature (423 K) does, however, represent a significant step forward in the development of a low-cost cyclohexanone production route.

CONCLUSIONS

A dilute palladium (1% w/w Pd)-on-MgO catalyst prepared by impregnation with $(NH_4)_2PdCl_6$ and activated by precalcination/low-temperature reduction, operating in the absence of thermodynamic limitations, selectively promotes the gas-phase hydrogenation of phenol to cyclohexanone with a selectivity in excess of 95% at 423 K. Both activity and selectivity drop at higher reaction temperatures as cyclohexanol is increasingly preferred. Steady-state conversion is readily achieved with no appreciable deactivation after extended (>55 h) catalyst use. The activated catalyst is characterised by a highly dispersed electron-rich metallic palladium phase ($D_{Pd} = 71\%$) which interacts with a support that is comprised of largely amorphous $Mg(OH)_2$ and crystalline needle-like MgO. There is also evidence of residual ammonium carbonate/ammonium hydrogen carbonate and chlorine on the surface. The high cyclohexanone selectivity is attributed to the nature of the surface activation of hydrogen (which is influenced by the charge density at the very small palladium crystallites) and/or phenol (through the –OH group) which leads to a preferential partial hydrogenation.

ACKNOWLEDGMENTS

This work has been supported in part by the Bundesminister für Bildung und Forschung (BMBF) under Grant 03D0028A0 and the Fonds der Chemischen Industrie. Assistance with experimental work provided by Dr. H. Hofmeister (Max-Planck Institute for Microstructure Physics Halle), M. Lucas (ACA Berlin), and S. Evert (ACA Berlin) is greatly appreciated. The authors thank the Max-Planck-Gesellschaft for use of the electron microscopy facilities and KataLeuna GmbH Catalysts/CRI for conducting the XRD measurements. E.J.S. acknowledges partial financial support from the British Council.

REFERENCES

1. Dodgson, I., Griffen, K., Barberis, G., Pignataro, F., and Tauszik, G., *Chem. Ind.* 830 (1989).
2. "Kirk-Othmer Encyclopedia of Chemical Technology" (M. Howe-Grant, Ed.), 4th ed., Vol. 1, p. 81. Wiley, New York, 1991.
3. Talukdar, A. K., Bhattacharyya, K. G., and Sivasanker, S., *Appl. Catal. A: Gen.* **96**, 229 (1993).
4. Gonzalez-Velasco, J. R., Gutierrez-Ortiz, J. I., Gutierrez-Ortiz, M. A., Martin, M. A., Mendioroz, S., Pajares, J. A., and Golfado, M. A., *in* "Preparation of Catalysts IV" (B. Delmon, P. Grange, P. A. Jacobs, and G. Poncelet, Eds.), p. 619. Elsevier, Amsterdam, 1987.
5. Itoh, N., and Xu, W.-C., *Appl. Catal. A: Gen.* **107**, 107 (1993).
6. Narayanan, S., and Krishna, K., *Appl. Catal. A: Gen.* **147**, L253 (1996).
7. Narayanan, S., and Krishna, K., *Catal. Today* **49**, 57 (1999).
8. Neri, G., Visco, A. M., Donato, A., Milone, C., Malentacchi, M., and Gubitosa, G., *Appl. Catal. A: Gen.* **110**, 49 (1994).
9. Mahata, N., and Vishwanathan, V., *Indian J. Chem. A* **37**, 652 (1998).
10. Chen, Y. Z., Liaw, C. W., and Lee, L. I., *Appl. Catal. A: Gen.* **177**, 1 (1999).
11. Rasband, W., NIH Image, Public Domain Software, U.S. National Institutes of Health, zippy.nimh.nih.gov.
12. Moulder, J. F., Stickle, W. F., Sobol, P. E., and Bomben, K. D., *in* "Handbook of X-Ray Photoelectron Spectroscopy" (J. Chastein and R. C. King, Jr., Eds.), p. 234 and references therein. Physical Electronics, Eden Prairie, 1995.
13. Shin, E.-J., and Keane, M. A., *J. Catal.* **173**, 450 (1998).
14. D'Ercole, A., Giamello, E., Pisani, C., and Ojamäe, L., *J. Phys. Chem. B* **103**, 3872 (1999).
15. Ito, T., Kuramoto, M., Yoshida, M., and Tokuda, T., *J. Phys. Chem.* **87**, 4411 (1983).
16. Ito, T., Murakami, T., and Tokuda, T., *J. Chem. Soc., Faraday Trans. 1* **79**, 913 (1983).
17. Hoffmann, P., Diwald, O., Sterrer, M., and Knözinger, E., Proc. XXXII. Jahrestreffen Deutscher Katalytiker, p. 51. DECHEMA Friedrichroda/Germany, 1999.
18. Zhang, G., Hattori, H., and Tanabe, K., *Appl. Catal.* **36**, 189 (1988).
19. Tsuji, H., Shishido, T., Okamura, A., Gao, Y., Hattori, H., and Kita, H., *J. Chem. Soc., Faraday Trans.* **90**, 803 (1994).
20. Hattori, H., *Chem. Rev.* **95**, 537 (1995).
21. Pearson, W. B., "Handbook of Lattice Spacings and Structures of Metals and Alloys." Pergamon Press, London, 1964.
22. Mojet, B. L., Kappers, M. J., Muijsers, J. C., Niemandsverdriet, J. W., Miller, J. T., Modica, F. S., and Koningsberger, D. C., *Stud. Surf. Sci. Catal.* **84**, 909 (1994).
23. Kappers, M., Dossi, C., Psaro, R., Recchia, S., and Fusi, A., *Catal. Lett.* **39**, 183 (1996).
24. Recchia, S., Dossi, C., Poli, N., Fusi, A., Sordelli, L., and Psaro, R., *J. Catal.* **184**, 1 (1999).
25. Lias, S. G., Liebman, J. F., Levin, R. D., and Kafafi, S. A., "NIST Standard Reference Database 25, Structure and Properties," Version 2.01, January 1994.
26. Rylander, P. N., "Catalytic Hydrogenation in Organic Synthesis," p. 194. Academic Press, New York, 1979.